Atomic Layer Deposition of Titania in Ordered Mesoporous Cerium Zirconium Oxide Thin Films: A Case Study

P. Cop, M. Göttlicher, J. Schörmann, C. Boissiere, A. Beyer, C. Becker, K. Volz, H. Over, B. Smarsly

To cite this version:

P. Cop, M. Göttlicher, J. Schörmann, C. Boissiere, A. Beyer, et al.. Atomic Layer Deposition of Titania in Ordered Mesoporous Cerium Zirconium Oxide Thin Films: A Case Study. Journal of Physical Chemistry C, 2019, 123 (20), pp.12851-12861. 10.1021/acs.jpcc.9b02069 . hal-03873181

HAL Id: hal-03873181

https://hal.sorbonne-universite.fr/hal-03873181

Submitted on 26 Nov 2022

HAL is a multi-disciplinary open access archive for the deposit and dissemination of scientific research documents, whether they are published or not. The documents may come from teaching and research institutions in France or abroad, or from public or private research centers.

L'archive ouverte pluridisciplinaire HAL, est destinée au dépôt et à la diffusion de documents scientifiques de niveau recherche, publiés ou non, émanant des établissements d'enseignement et de recherche français ou étrangers, des laboratoires publics ou privés.

Atomic Layer Deposition of Titania in Ordered Mesoporous Cerium Zirconium Oxide Thin Films: A Case Study

P. Cop,[†,‡] M. Göttlicher,[†,§] J. Schörmann,[‡,§] C. Boissiere,[∥] A. Beyer,[⊥] C. Becker,[⊥] K. Volz,[⊥] H. Over,[*,†,‡] and B. M. Smarsly[*,†,‡]

[†]Physikalisch-Chemisches Institut, Justus-Liebig-Universität, Heinrich-Buff-Ring 17, D-35392 Giessen, Germany

[‡]Center for Materials Research and [§]I. Physikalisches Institut, Justus-Liebig-Universität, Heinrich-Buff-Ring 16, D-35392 Giessen, Germany

[∥]Laboratoire Chimie de la Matière Condensée de Paris Collège de France, 11 Place, Marcelin Berthelot, 75005 Paris, France

[⊥]Department of Physics and Materials Science Center, Philipps-Universität Marburg, Hans-Meerwein-Straße 6, D-35032 Marburg, Germany

INTRODUCTION

Recent advances in the preparation of nanostructured materials revealed particular interests in metal/oxide and oxide/oxide nanostructures. Merging the unique characteristics of two materials into one system can be favorable, especially for metal oxides. The combination of two different metal oxides can enhance the overall material properties, for instance, in gas sensing, electrochemical energy storage, medical treatment, and (photo/electro) catalysis[1−9] due to synergetic effects. Such effects are related to the interface between the two materials affecting the formation of oxygen vacancies, stabilizing desired ion species, or, in general, enhancing the catalytic activity and stability.[10−17] In addition, by tailoring the layer thickness of the active metal oxide species, the properties of thin layers of the oxide(s) may differ from the bulk counterpart. Core−shell nanostructures are one important example using the benefits of two metal oxides by maximizing the interfacial surface area between the core and shell metal oxides. For instance, a ZnO shell on SnO_2 nanorods enhances the selectivity in H_2 gas sensing.[18] Single-crystalline ZnO nanorods covered with a porous MnO_2 shell possess improved supercapacitor performance.[19] Dumesic and co-workers deposited Nb_2O_5 layers into the pores of mesoporous silica (SBA-15) and studied this hybrid catalyst in the gas-phase dehydration of 2-propanol confirming the superiority of their catalyst in activity and stability compared to commercial Nb_2O_5.[20] By changing the thickness of the γ-Fe_2O_3 shell layers on a Fe_3O_4 core, the magnetic properties depending on the temperature were modified for its usage in magnetic hyperthermia treatments.[21] Artiglia et al. demonstrated the preparation of CeO_2/TiO_2 core/shell structure stabilizing the Ce^{3+} species on the TiO_2 surface.[10] In that study, by changing the thickness of the coating layer with a wet impregnation method, the ratio of Ce^{3+}/Ce^{4+} was tailored. However, this kind of deposition method is difficult to control and does not provide a homogeneous and conformal coating of the core material, for

instance, because the nanoparticles are attached to each other in an uncontrollable fashion and also might move during deposition, resulting in an inhomogeneous coating with the second metal oxide. By contrast, in mesoporous thin films, the crystalline metal oxide structure is stabilized and completely accessible. The impregnation of a continuous mesoporous metal oxide framework is therefore fundamentally more suitable in comparison to corresponding nanoparticles.

Besides the usage of impregnation methods such as co-condensation,[22] grafting,[23,24] and wet impregnation,[25,26] atomic layer deposition (ALD) is a promising alternative for the deposition of defined layers with nanometer-sized thickness. While physical and chemical vapor deposition techniques are able to deposit a variety of metal oxides on planar substrates, ALD allows the coating of conformal layers even on complex substrate morphologies by separating the gas−solid reactions with purging steps and therefore building up the film layer by layer.[27−31] This self-limiting nature of the ALD enables the atomic-level control of the formed layer in the interior of a nanopore according to the desired physicochemical effects.

While the deposition in porous structures with pore sizes above 50 nm is easily confirmed by using electron microscopy techniques, the difficulty of validating thin conformal coatings arises with decreasing pore sizes. In the last years, various complex porous substrates such as SBA-15,[20] aluminum oxide membranes,[32−34] carbon,[35] and zeolites[36] were coated with active species using ALD to study the effect of the deposition layers on the specific material properties. Kraffert et al. demonstrate the shift of the crystallization temperature of ferrihydrite films to higher temperatures using coatings of alumina and silica on the mesopore surface.[37] Detavernier et al. presented the possibilities to prove the conformal coating of mesoporous thin films with pore size less than 10 nm in a tutorial review.[38] They presented in situ X-ray fluorescence and ellipsometric porosimetry (EP) investigations not only on the validation of the deposition in the interior pore layers, but also on the formation of metal oxide layers on top of the substrate. In continuous studies, Detavernier's group used the in situ EP technique to investigate the ALD growth of TiO_2 in mesoporous silica films and HfO_2 in TiO_2 films with ink-bottle mesopores.[39,40] The latter revealed that the limit of tuning the pore size in these mesoporous materials is determined by the diameter of the smallest pores connecting the bigger pore layers and hence, literally being the "bottleneck" of the ALD. This was additionally proven by the same group using in situ synchrotron-based grazing-incidence small-angle X-ray scattering (SAXS) on Pluronic F127-templated titania thin films.[41]

However, the mesoporous thin films templated by the block copolymer Pluronic F127 only yielded a nonordered structure of mesopores with small pore sizes below 8 nm and connecting channels of nonuniform sizes and shapes. Hence, transition-metal oxides with well-ordered mesopore arrangements as well as larger mesopore diameters (i.e., >10 nm) are desirable, to study size effects of crystalline metal oxide coating layers on the pore surface. Consequently, with defined pore shape, connection, and size, the details of the ALD-based deposition can be studied more accurately and systematically than for nonordered porous films because changes in the pore size and accessibility can be detected and quantified more reliably and can thus be related to deposition parameters. By using specific block copolymers, our group has achieved mesoporous

structures with pore sizes between 12 and 25 nm forming a three-dimensional (3D) network of spherical mesopores connected by smaller channels.[41−45] The cubic ordered structures with pore sizes around 14 nm were synthesized using the diblock copolymer poly(isobutylene)-*block*-poly-(ethylene) oxide referred to as PIB_{50}-*b*-PEO_{45}. The template was already used to prepare various metal oxides, e.g., TiO_2,[42,43,42,43] indium tin oxide,[44] Al_2O_3,[45] and $Ce_xZr_{1−x}O_2$,[46] which showed a favorable ordered structure in its 1:1 mixture $Ce_{0.5}Zr_{0.5}O_2$ (CZO), making it a good model system to study the incorporation of TiO_2 into the mesoporous structure using ALD. Furthermore, we have chosen CZO and TiO_2 as model case, as TiO_2/CeO_2 material systems have been proven to be promising catalysts for various reactions, for instance, in the selective catalytic oxidation of NH_3 to N_2[47] and catalytic reduction of NH_3 to NO[48] (SCR). Spectroscopic studies of the interfacial sites of these binary oxides were investigated by Fang et al.,[49] revealing an enrichment of anatase on the interfacial sites as the Ti^{4+} substitutes Ce^{4+} in the cubic CeO_2 lattice. Huang et al.[50] successfully prepared $CeO_2@TiO_2$ core−shell nanostructures with an enhanced catalytic activity, stability, and superior tolerance against SO_2 and H_2O for low-temperature SCR of NO_x using NH_3. The reason for selecting TiO_2/CeO_2 is ascribed to the high mobility of lattice oxygen inside the catalyst and thus the increased oxygen storage capacity, which can be further raised by incorporating zirconium ions in the ceria lattice.[51] Since the CZO-TiO_2 interface thus endows these two oxides with beneficial properties, we chose mesoporous CZO thin films as substrate within defined layers of TiO_2, which are deposited using ALD. Using TiO_2 as the oxide to be deposited by ALD is favorable, as its growth using $TiCl_4$ and H_2O is widely studied[52−54] and shows sufficiently different properties compared to the CZO mesoporous film, allowing for its detection within the final hybrid films.

As the main goal, in this work, ordered mesoporous CZO thin films are prepared and infiltrated with TiO_2 using the ALD technique, to study the incorporation process inside the mesopores (see Figure 1). The study also addresses the question whether the bigger, spherical mesopores (ca. 15−20 nm in diameter) can be impregnated, even though the smaller channels between the spherical mesopores may limit the amount of deposited oxide on the pore surface. The films are analyzed by several state-of-the-art methods, using scanning
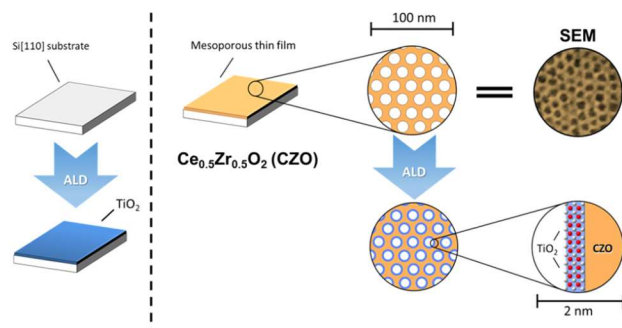
Figure 1. Schematic overview of the strategy for studying the atomic layer deposition (ALD) of thin layers of TiO_2 in the mesoporous matrix of $Ce_{0.5}Zr_{0.5}O_2$ thin films with pore sizes of 13 nm verified by top-view scanning electron microscopy (SEM) recordings. In addition, pure silicon [110] substrates were coated with TiO_2 to verify the growth rate.

electron microscopy (SEM) and high-resolution (scanning) transmission electron microscopy (HR(S)TEM) to visualize the mesoporous structure, while laser ellipsometry, X-ray reflectometry (XRR), and time-of-flight secondary-ion (SI) mass spectrometry (ToF-SIMS) investigations give information about the TiO_2 content inside the porous network. Finally, X-ray diffraction (XRD), selected area electron diffraction (SAED), and the evaluation of the atomic planes in the HRTEM images are used to determine the crystal structure. Ellipsometric porosimetry was used to study the filling of mesopores upon consecutive ALD within the mesoporous films. This study is thus intended to demonstrate if and how typical laboratory characterization techniques can be used ex situ to study and validate the ALD within the interior pore structure, providing a guide to ALD-based growth of different transition-metal oxides on crystalline mesoporous substrates in general. In particular, special emphasis is put on validating the analysis of the growth/deposition of TiO_2 by using complementary techniques, each of them providing a different type of information. Furthermore, in the future, the presented mesoporous systems will allow investigating the influence of the ALD layer thickness on the physicochemical and catalytic properties, such as the catalytic performance in the SCR of NO_x using NH_3.

EXPERIMENTAL

Preparation of the Mesoporous Thin Films. The fabrication of mesoporous CZO thin films[46] using an evaporation-induced self-assembly (EISA) approach was based on a precursor solution, $CeCl_3 \bullet 7H_2O/ZrOCl_2 \bullet 8H_2O/$ PIB_{50}-b-$PEO_{45}/H_2O/$2-methoxy-ethanol/ethanol, mole ratio 0.5:0.5:0.005:18:10:35. PIB_{50}-b-PEO_{45} (50 mg; BASF, Ludwigshafen, Germany) was added to 1 mL of ethanol (99.8%, Merck), while 110 mg of $CeCl_3 \bullet 7H_2O$ (98%, Sigma-Aldrich) and 92 mg of $ZrOCl_2 \bullet 8H_2O$ (99.9%, Alfa Aesar) were dissolved in 0.5 mL of ethanol and 0.5 mL of 2-methoxy-ethanol (99%, Alfa Aesar) in both cases at room temperature. Both mixtures were treated in an ultrasonic bath for 30 min at 35 °C and 80 kHz. The solutions were cooled down to room temperature and mixed together. After 5 min stirring, 0.1 mL of distilled H_2O was added to the solution to start the hydrolysis process.

After a stirring time of 90 min, the solution was freed from agglomerates using 0.2 μm syringe filters. A small amount (100 μL) of this solution was taken and deposited on a 2 in. Si[110] wafer rotating at 1000 rpm for 60 s using a spin Coater Kit SCK-200P from Instras Scientific. The relative humidity inside the chamber was kept constant at 20%, utilizing a custom-made glass enclosure. The films were treated at such low relative humidity for additional 3 min and then transferred to a preheated furnace at 130 °C to force the solvent to evaporate. Afterward, the films were aged at 300 °C in air for 12 h to remove the structure-directing agent. In the final step, the coated substrates were annealed to 600 °C in air to obtain crystalline CZO thin films. In a final step, the films were cut into 1 × 1 cm^2 pieces for the ALD procedure.

ALD. Si[110] wafers and the mesoporous CZO thin films were coated with TiO_2 using a PicoSun R200 ALD reactor. The deposition was performed using a reactor temperature of 200 °C with an intermediate space flow between the reactor and the vacuum pump of 150 sccm nitrogen, while 80 sccm nitrogen was carried through the precursor lines. A typical ALD cycle consisted of a 0.1 s $TiCl_4$ pulse followed by a 35 s

purging step with nitrogen. Afterward, H_2O was pulsed for 0.1 s into the reaction chamber. A last purging step of 35 s using nitrogen completed the cycle (see Figure 2). To achieve a
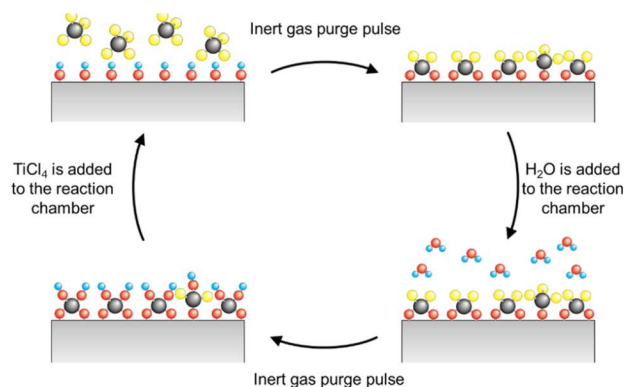

Figure 2. Schematic overview of the ALD process for preparing thin films of TiO_2. The precursors are $TiCl_4$ and H_2O, while nitrogen was used as the inert gas.

higher dwell time of the precursor in the reaction chamber allowing the precursor to reach every pore in the complex oxide, the PICOFLOW diffusion enhancer was applied. Within 1.5 s, the flow rate of the carrier gas was throttled to 40 sccm and the valve at the end of the reaction chamber was closed. After 1.3 s, the precursor pulse of 0.1 s was initiated. In the next 30 s, the nonadsorbed precursor and possible byproducts were flushed out of the chamber. The thin films were coated using 0, 5, 10, 25, 50, 100, 150, and 200 cycles, which are labeled as 0c, 5c, ..., 200c in the following work.

Characterization of the Coated and Noncoated Mesoporous Thin Films. Scanning electron microscopy (SEM) images were recorded using the model Merlin by Zeiss with an acceleration voltage of 2 keV and a current of 50 pA. To increase the conductivity of the samples, the films were sputtered with platinum for 10 s with an applied current of 40 mA. The acquired mesopores were sized by using the program Fiji.app. For every determined pore size, the diameters of 100 mesopores were measured. The crystalline phases of the thin films were studied by grazing-incidence X-ray diffraction (GI-XRD) acquired from a PANalytical X'Pert^3 MRD diffractometer. An incidence angle of $\omega = 0.25°$ was set at which the samples were scanned in the 2θ range of 20−70° with a scan speed of 0.6° min^{-1} and a step size of 0.01° using 2θ mode. The crystallite sizes were calculated applying the Scherrer equation[55] on the wide-angle reflections. The X-ray reflectivity measurements were performed on a PANalytical X'Per^3 MRD diffractometer. Here, the films were investigated using $2\theta/\omega$ mode in the incident angle scan range of 0.1−2°. The data analysis was performed utilizing the corresponding software X'Pert Reflectivity. All of the X-ray experiments were done using Cu Kα radiation. The thicknesses of the films were determined using a SE400adv laser ellipsometry by Sentech, which is equipped with a HeNe laser (633 nm). The samples were measured at the specific angle of 70° assuming a two-model system consisting of the CZO film and the Si[110] substrate. For the time-of-flight secondary-ion mass spectrometry (ToF-SIMS), a ToF-SIMS 5-100 model by IonTOF GmbH was used with an acceleration voltage of 25 keV for the Bi(I) primary-ion source. The depth profiles were recorded using Cs ions at 500 eV and a current of 50 nA. Only 50 × 50

μm² of the generated 100×100 μm² crater was analyzed with a resolution of 256×256 pixels². The measurements were carried out under charged compensation.

TEM samples were prepared by conventional mechanical grinding followed by argon ion milling until electron transparency in a GATAN precision ion polishing system. The STEM measurements were carried out in a CS-corrected JEOL JEM 2200FS operating at 200 kV. The high-angle annular dark-field signal was utilized for the imaging. This signal provides z-contrast, which allows to differentiate between the different materials in the samples.[56]

For the ellipsometric porosimetry, the refractive index as well as the thickness of films were measured using a variable-angle spectroscopic ellipsometer (VASE) M2000DI from Woollam. The data were recorded with an incident angle of 70°, and the thickness and refractive index were obtained at 700 nm by using a Cauchy model[57] for fitting ellipsometric data between 450 and 1000 nm wavelengths. The films were exposed to different relative pressures of ethanol achieved by mixing ethanol and dry air in different ratios using two mass flow controllers. While increasing the relative pressure of ethanol from 0 to 100% in 20 min, the isotherm points were recorded every 20 s. The calculation of the pore volume was then determined by a previously reported procedure.[58]

RESULTS AND DISCUSSIONS

The mesoporous CZO thin films acting as the model system for the atomic layer deposition were prepared using solutions of the corresponding metal salts ($CeCl_3 \bullet 7H_2O$ and $ZrOCl_2 \bullet 8H_2O$) and the structure-directing block copolymer PIB_{50}-b-PEO_{45}.

In this so-called EISA approach,[59] the inorganic precursor and the organic template were put together in a mixture of ethanol and 2-methoxy-ethanol. Via spin coating, the solution was deposited on a partially oxidized Si[110] substrate to produce thin films with initial thicknesses of around 100 nm. A following annealing step decomposed the polymeric template and induced the crystallization eventuating in the desired mesoporous CZO thin film with a cubic arrangement of the mesopores, which was proven by SAXS measurements and SEM recordings in previous works.[46,60] The obtained mesoporous structure depends on the used block copolymer. In this work, 14 nm mesopores were obtained, which is common for PIB_{50}-b-PEO_{45}.[42,44,45] Furthermore, interconnecting channels between two mesopore layers perpendicular to the substrate are present (see the SEM image in Figure 1) allowing a gaseous precursor used in the ALD to reach the entire surface of the mesopore network.

To calculate the growth rate of TiO_2, Si[110] wafers were coated with TiO_2 by ALD using the same deposition parameters as using the mesoporous samples. The growth rate of TiO_2 can be determined using laser ellipsometry by measuring the thickness after different numbers of applied ALD cycles (Figure 3). However, as the thicknesses after 5, 10, 25, and 50 cycles are below the detection limit of the ellipsometric analyses, only 100, 150, and 200 cycles are taken into account for the calculation of growth rate. The resulting growth rate for TiO_2 using the diffusion-enhancer function of our ALD setup is 0.067 nm per cycle, i.e., it is linear. However, the deposition rate for low number of cycles was reported to follow a nonlinear trend.[61] In the beginning, the deposition is supposed to be aggravated, as the precursor has to attach to the hydroxyl group on the surface of the silicon substrate, while
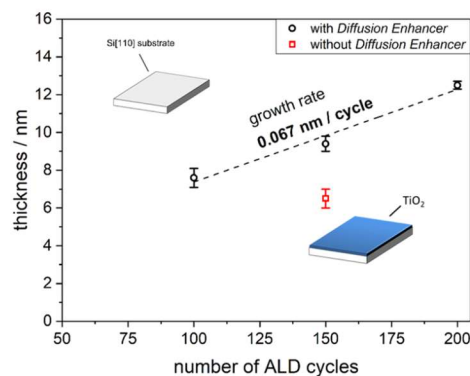

Figure 3. Thickness of the TiO_2-deposited Si[110] substrates depending on the number of ALD cycles. The dashed line illustrates the assumption concerning the growth rate. Additionally, the obtained thickness after 150 cycles with (black) and without using the diffusion-enhancer function (red) is shown.

after one complete cycle, the precursor reacts with Ti$-$OH groups. This assumption is, of course, only the case under the supposition that $TiCl_4$ chemisorbs on the substrate surface as a perfect monolayer entirely. The diffusion-enhancer function increases the dwell time of the titanium precursor $TiCl_4$ and H_2O in the ALD reactor and, hence, the contact with the substrates. It allows the precursor to chemisorb on more active spots than without using the function and therefore covering more area of the substrate and leading to a higher surface saturation per cycle. Hence, the growth rate is increased. Especially with complex substrates like mesoporous thin films, this higher resting time facilitates the diffusion in the porous network and allows coating even the lowermost pore layer. However, when transferring the growth rate obtained by coating the Si wafers to the deposition on mesoporous thin films, one has to take into account that a different roughness of the substrate influences the growth rate as shown by Langner et al.[62]

Using different numbers of ALD cycles, TiO_2 was then deposited on the mesoporous CZO thin films. The changes of thickness and refractive indices depending on the number of ALD cycles were investigated using laser ellipsometry (see Figure 4). While the thickness of the CZO films after 5 and 10 cycles remains constant at 92 nm, the refractive index of these films increases. After 25 cycles, the film slightly raises in thickness and refractive index, which is continued even for 50 cycles. For 100, 150, and 200 cycles, the thickness increases faster eventuating in a 13 nm coating on top of the mesoporous film. Although a direct differentiation of the original film and the added layer is not possible, the results indicate a TiO_x layer forming especially with higher cycle counts. Moreover, the alteration of the refractive index depending on the cycle number shows a saturation, and no significant change of the refractive index is observed after 50 cycles. Even with a growing TiO_2 layer on top, the refractive index remains constant. The resulting refractive index of around 2.14 between 50 and 200 cycles is still lower than the one of dense CZO[63] and anatase determined by the ellipsometric studies of the coated silicon substrates suggesting a mixture of CZO and TiO_2 for the measured films. The rising refractive index for the films after 5, 10, and 25 cycles reveals a possible deposition in the mesopores, as no significant thickness rise was detected. A decrease in the pore size and therefore in porosity due to TiO_2 attaching to the pore surface
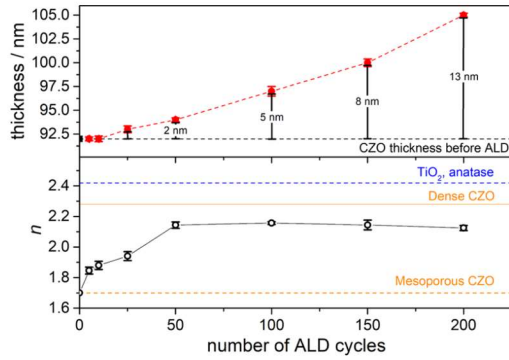
Figure 4. Thickness (top) and refractive index (bottom) of the mesoporous CZO film before and after applying a certain number of ALD cycles, determined by laser ellipsometry performed using $\lambda = 633$ nm. The difference in size between the sample before and after the deposition via ALD is also displayed as well as the refractive index of anatase (blue), dense (solid line), and mesoporous (dashed line) CZO (orange). The former is based on ellipsometric studies of the deposited TiO_x film on Si[110] substrates.

raises the refractive index above the initial index of refraction of the mesoporous CZO films.

To prove the existence of TiO_2 inside the mesopores, depth profile analyses of the films using ToF-SIMS were carried out. Secondary ions like CeO^-, ZrO^-, TiO^-, as well as Si^- anions were detected and help to clarify the location of these species inside the film. By using Cs ions as the sputter source, the film was skimmed and the subjacent layer was analyzed concerning these ions. Following this procedure, depth profiles were recorded and are shown exemplarily in Figure 5 for the films after 5, 25, and 150 cycles. Additionally, the untreated CZO

film was sputtered as long as the silicon was reached. An investigation by a surface profilometer revealed a thickness of 92 nm, which is in good agreement with the results of the ellipsometric studies. As seen in Figure 5, the signals of CeO^- and ZrO^- proceed parallel to each other, indicating the equal distribution of these species in the film. The different intensity derives from the ion-specific ionization energy of the analyzed anions. The homogeneity of the TiO_x species inside the film is proven by considering the TiO^- count slope, which is also parallel with the CZO species CeO^- and ZrO^- slope. Moreover, all of the three secondary ions decrease equally when reaching the silicon substrate pointed out by the Si^- signal. With higher number of ALD cycles, the TiO^- counts increase, revealing a higher amount of Ti in the film. It is also observed that after 150 cycles, there is a thin layer of TiO_x present on top of the CZO film, which is in good agreement with the laser ellipsometric studies. Furthermore, the depth profiles show that the ablation rate differs by ionic species. While the film after five ALD cycles needs only 120 s of sputter time to be completely removed, the sample after 150 cycles requires already 230 s. As all samples were analyzed using the same instrumental parameters, a semiquantitative analysis of the TiO_x content is possible. Hence, the signal ratio of TiO^- to ZrO^- depending on the number of ALD cycles is in relation to the TiO_x amount in the film and was calculated after a sputter time of 50 s for every sample (Figure 5). Here, the saturation curve for the TiO^-/ZrO^- ratio is similar to the dependence of the refractive index as a function of the number of ALD cycles. While the TiO_x content raises within the first 50 cycles inside the mesoporous films, it remains nearly constant within the films for the following cycles. This finding indicates that the
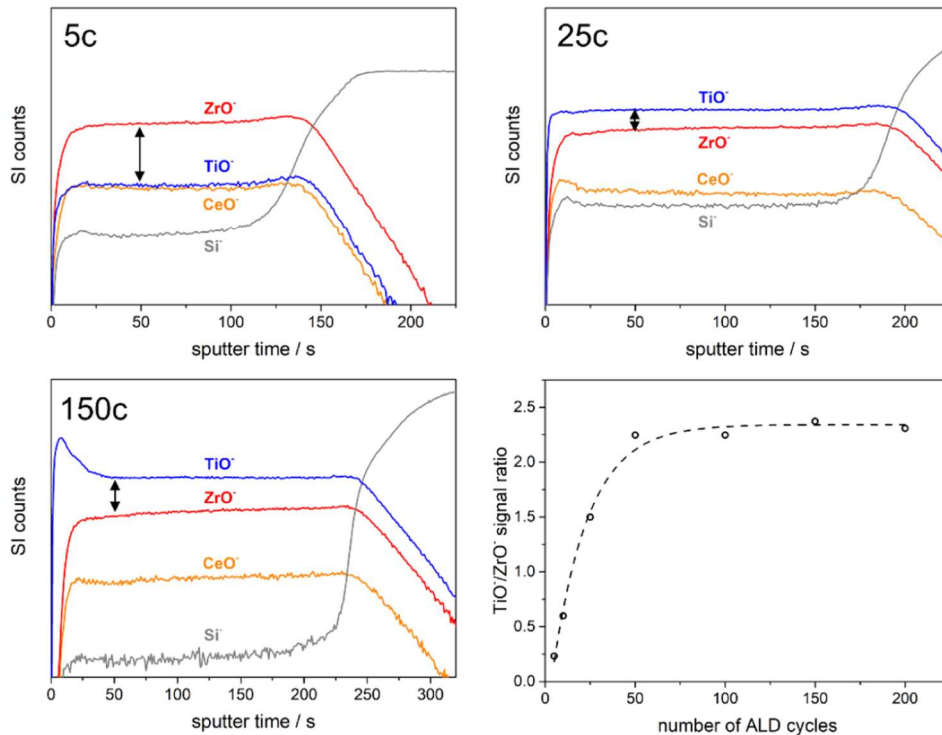

Figure 5. ToF-SIMS depth profiles of the mesoporous CZO film after 5, 25, and 150 ALD cycles. Next to the ions derived from the thin film (TiO^-, ZrO^-, and CeO^-), the signal from the utilized silicon substrate (Si^-) is depicted by plotting the secondary-ion (SI) counts logarithmic dependent on the sputter time. In addition, the signal ratio of TiO^- to ZrO^- at 50 s of sputtering in relation to the ALD cycles is shown.

mesopores seem to be either completely filled or coated in a way that diffusion to lower pore layers is impossible.

Further deposition cycles at the given ALD conditions only add TiO_x layers on the top of the film, implied by the TiO^- signal maximum before reaching the mesoporous CZO network for the film after 150 cycles. As after every sputter step an area of $50 \times 50 \ \mu m^2$ was investigated, 3D topographical images were calculated as shown in Figure 6 for the uncoated.
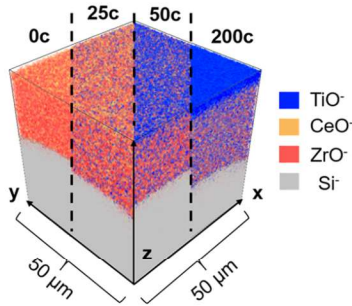

Figure 6. Three-dimensional (3D) topographic images based on the ToF-SIMS depth profiles for the untreated mesoporous CZO films, as well as after 25, 50, and 200 ALD cycles. The z axis corresponds to the sputter time.

CZO film, as well as after 25, 50, and 200 cycles of the atomic layer deposition. Here, the layer on top of the CZO film is even more evident, while the content of TiO_x inside the film stays nearly constant between the samples after 50 and 200 ALD cycles. This observation indicates again that the pores in the sublayers are not accessed by the gaseous ALD precursors and only a top layer on the CZO is growing, which differs slightly from the obtained thickness on silicon substrates. The disparity occurs as the mesoporous CZO and Si substrates are quite different concerning their roughness, material properties, as well as the specific surface area. The latter gives diffusion processes a higher impact on the growth rate.

To verify the pore arrangement and the TiO_2 deposition on the topmost pore layer, the films were analyzed using SEM (see Figure 7). The uncoated sample reveals an ordered array of mesopores with ca. 14 nm diameter (top view), which shrink with increasing number of ALD cycles. As the same procedure for a Pt overcoat was used to increase the conductivity of the analyzed samples, the determined pore
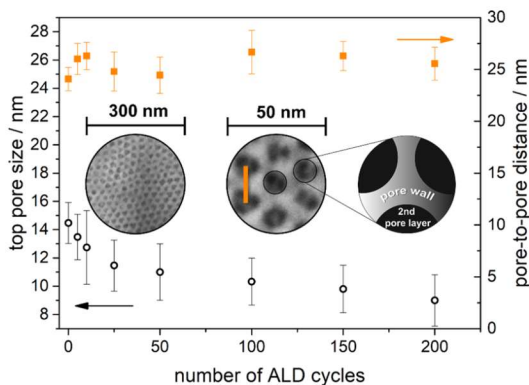

Figure 7. Pore size (black circles) and pore-to-pore distances (orange rectangles) based on the SEM images for the uncoated and coated mesoporous CZO using different numbers of ALD cycles.

size may be a bit smaller than the actual one without an overcoat. Similar to the ToF-SIMS and ellipsometry results, the mesopore size drops significantly until 50 cycles and then slowly decreases down to 9 nm in diameter after 200 ALD cycles (see Figure 8), whereas the pore-to-pore distance remains almost constant for every sample at 25 nm. By considering the shrinkage of the mesopore size, the width of pore walls enlarges with the increasing number of ALD cycles.

However, in contrast to the assumption based on the ToF-SIMS conclusion that the pores are possibly filled, mesopores are still visible according to the SEM images. In general, SEM analysis reveals only the film from a top view (see Figure 7). While the second pore layer is visible in the uncoated CZO films even up to 10 cycles, it is not detectable from 25 cycles onward. This observation implies that the interconnecting channels between the pore layers are filled preventing the access of the gaseous ALD precursors to the inner pore surfaces. As the ToF-SIMS and ellipsometric studies suggest a TiO_x layer thickness of around 13 nm after 200 cycles, we assume the layer was deposited as pillars around the existing mesopores. Hence, in a top view, the mesopores are still visible, but are decreased only slightly in their lateral diameter as the pillars coalesce slowly.

The thin films were also investigated using X-ray reflectivity (see Figure 9). Due to the present ordered cubic arrangement of the mesopores, the (111) Bragg signal is visible next to the critical angle and the common fringes. The critical angle shifts too higher s-values or incident angles for higher ALD cycles. As the critical angle is directly related to the density of the materials, a density increase from 1.9 to 3.1 g cm^{-3} indicates the filling of the mesopores, while these values are much lower than the crystallographic densities of pure CeO_2 (7.3 g cm^{-3}), tetragonal ZrO_2 (6.1 g cm^{-3}), or TiO_2-anatase (3.89 g cm^{-3}). Obviously, these low density values are due to the significant mesoporosity of the CZO films as well as in the presence of small crystallites with a few nanometers in diameter decreasing the density in comparison to the bulk equivalent. However, the enhancement in the density being stronger up to 50 cycles than for 100, 150, and 200 cycles implies the impregnation of the inner mesopores until 50 cycles. Hence, the mesoporosity decreases and the density increases accordingly, which is in good agreement with the refractive index results based on the ellipsometric measurements (Figure 4). Furthermore, the visible Bragg maximum related to the cubic pore arrangement perpendicular to the substrate plane broadens after 5, 10, and 25 ALD cycles and vanishes after undergoing 50 growth cycles. As the maximum originates from electron density differences and its width corresponds to the variation of these difference values, the original mesopores surrounded by pure CZO are coated with a different material, e.g., TiO_2, on the pore surface. After 50 cycles, the interconnecting channels are filled and the gaseous ALD precursors can only reach the topmost pore layers. The recurring electron density disparity necessary for the Bragg signal to be detected disappears and hence the signal vanishes, as seen in Figure 9. As the Bragg signal derives from the cubic arrangement of the mesopores, the visible signal corresponds to the (111) reflection. By multiplying the reciprocal s value of the slope maximum of the different samples by the square root of 3, the XRR data reveal a pore-to-pore distance in the z-direction of around 18 nm. Due to the heat treatment of the film during its preparation, the mesopores undergo an ellipsoidal deformation and overall shrinkage in the direction perpendicular to the substrate level,
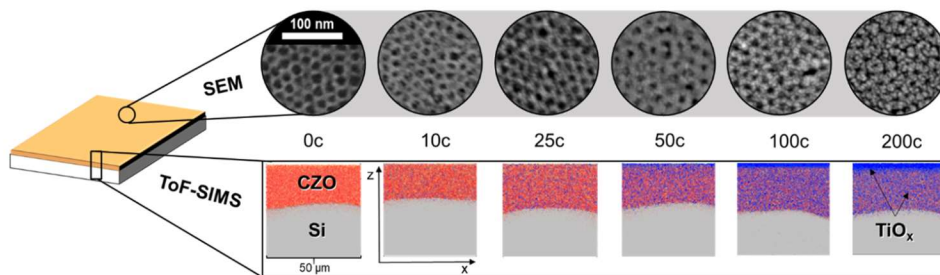
Figure 8. Differentiation of the SEM and ToF-SIMS investigations for the uncoated and coated mesoporous CZO films. The SEM images reveal morphological changes of the porous structure from a top view of the film (top), while the ToF-SIMS depth profile shows the secondary-ion distribution inside the whole film (bottom).
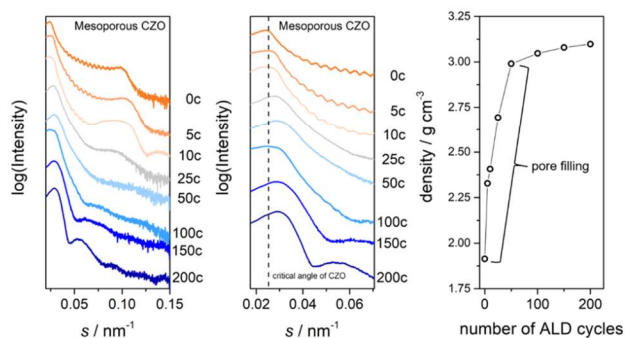

Figure 9. XRR data of the CZO mesoporous thin films before and after depositing TiO$_2$ via ALD using different numbers of growth cycles, and the calculation of the average density based on the position of the critical angle.

resulting in a smaller pore-to-pore distance in comparison to the obtained values in the *x*- and *y*-directions, respectively, as presented in Figure 8, based on the SEM investigations (around 25 nm). Finally, the second maximum observed for the sample after 200 ALD cycles is a fringe and was used together with the third maximum/second fringe to determine the thickness of the TiO$_x$ top layer to be 12 nm, which is in accordance with the ellipsometric result providing 13 nm.

To analyze the mesoporosity, nitrogen physisorption measurements were performed on a 500 nm film prepared by repetitive coatings (see Figure S1). The investigation reveals a pore size distribution with an average size of around 13 nm, with a second maximum of around 5−6 nm. The latter can be assigned to the interconnecting channels and seem to be the limiting factor for the ALD, which is in good agreement with the work of Dendooven et al.[40] However, after five growth cycles via ALD, the adsorbed volume already shrinks down to 50% in comparison to the uncoated film. After 10 cycles, the pore volume remains constant implying the filling of the interconnecting channels, preventing further deposition inside the mesopores. This contradicts the observation made via ToF-SIMS and laser ellipsometry. A possible reason for this result is a stacking mismatch of the various mesoporous CZO layers caused by the repetitive coating resulting in a different model system from the single-coated CZO films. Unfortunately, using the given method without multilayer coating, only thicknesses around 100 nm are achieved, which is too thin for the nitrogen physisorption measurements.

To determine the relative pore volume defined as the volume fraction of pores in an otherwise presumed dense film, environmental ellipsometric porosimetry (EEP) analyses were performed on the coated thin films. The results are shown next

to the measured refractive index at 700 nm in Figure 10. As expected, the relative pore volume quickly decreases from
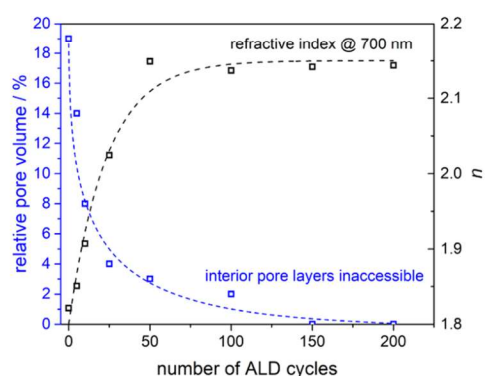

Figure 10. Refractive index *n* at 700 nm and relative pore volume determined by ellipsometric porosimetry (EP) dependent on the number of ALD cycles. The dotted lines serve as a guide to the eye to illustrate the curve slope.

around 20% for the uncoated sample with increasing number of ALD cycles and reaches less than 4% ($\pm$2%) above 50 cycles. This is in good agreement with the findings of the laser ellipsometry and ToF-SIMS studies as after 50 cycles the pores are not accessible anymore for the gaseous ALD precursor as well the solvent used in the EEP measurement. The interconnecting channels are filled and prohibit the access to the pores in the depth. While the mesopore volume can be determined with reasonable precision, the evaluation of the pore size distribution was associated with quite high fundamental uncertainty: the pore-size-dependent condensation of the used fluid (ethanol) within the mesopores is substantially superimposed by the wetting of the oxidic surface by ethanol. Since the wettability in general considerably affects the calculation of pore sizes (see, e.g., the Kelvin equation) and since the wetting behavior is unknown in this particular case, no pore size distribution is shown based on EEP (see EEP data in Figure S2).

While all of these analyses suggest an impregnation of the mesopores, GI-XRD measurements were performed on the sample to study the presence of crystalline TiO$_2$. The results are shown in Figure 11 for the uncoated films as well as the films after the ALD procedure. The cubic structure of Ce$_{0.5}$Zr$_{0.5}$O$_2$ based on the reference pattern is observed for every sample, while the sharp reflections can be assigned to the Si[110] substrate. Using the Scherrer equation, the average crystallite size for CZO is 7 nm. However, there is no evidence of a TiO$_2$ crystal phase. When annealing the sample after the
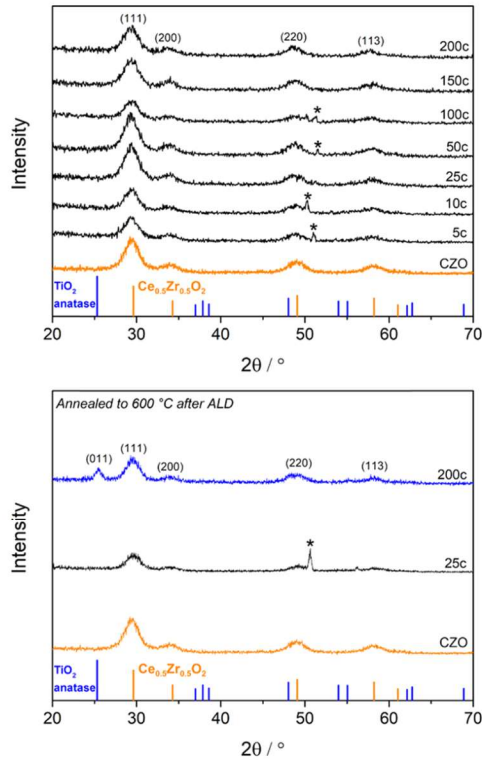
Figure 11. (Top) X-ray diffraction pattern of the mesoporous CZO thin film before and after the ALD using different amount of cycles. (Bottom) X-ray diffraction pattern of the mesoporous thin film after 0, 25, and 200 ALD growth cycles, followed by an annealing step to 600 °C. In both cases, the reference pattern for the cubic lattice of $Ce_{0.5}Zr_{0.5}O_2$ (ICDS 98-016-1650; orange) and anatase (ICDS 98-015-4604) are shown. The reflections marked with an asterisk derive from the Si[110] substrate.

Figure 12. High-resolution STEM images of the untreated mesoporous CZO thin film before (a) and after 150 TiO$_2$-ALD cycles (b). Moreover, the FFT calculations based on the atomic lattices are displayed within the STEM images (a) and (b). EDX measurements of the film after 150 cycles are additionally presented for Zr, Ti, and Si (c).

deposition procedure to 600 °C for 10 min and cooling down to room temperature, the (011) reflection of anatase is visible for the coated film after 200 cycles but not after 25 cycles. This observation can be explained in two ways: On the one hand, the amount of presumably amorphous TiO$_x$ in the pores crystallizing into anatase is insufficient for the XRD investigations to be detected. On the other hand, only the 13 nm TiO$_x$ layer on top of the film shown by ToF-SIMS and laser ellipsometry can crystallize, forming anatase after the postdeposition heating step.

Finally, the films were analyzed using transmission electron microscopy (TEM, Figure S3) and high-resolution STEM (HRSTEM) to visualize the TiO$_x$ coating of the mesoporous CZO network. The results are presented in Figures S4 and 12a−c. The brightness in these images derives from the z-contrast, meaning that compounds with a higher atomic number appear brighter. As shown in Figure 12a, the film consists of distributed bright and dark spots, in which the latter can be assigned to the mesopores. In this cross-sectional view of the mesoporous film, the thickness is determined as 94 nm, with a 2.7 nm thick SiO$_2$ layer on top of the silicon substrate. By comparing the HRSTEM images of the films before and after 150 ALD cycles, the latter appears to have a reduced contrast implying the filling of the mesopores. To distinguish between TiO$_x$ and CZO, local energy-dispersive X-ray (EDX) measurements were performed. The results shown in Figure 12c illustrate the distribution of the elements Ti, Zr
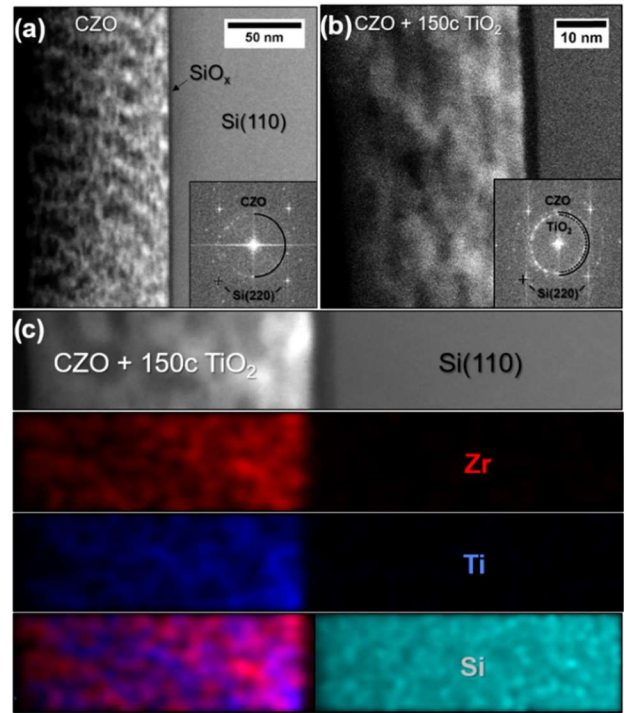
(representative for the CZO film), and Si. The overlay of the Ti and Zr signals demonstrates the complementary distribution of these elements inside the film, giving direct evidence that the pores are indeed coated with Ti or TiO$_x$, respectively. Although these images do not provide information on the interconnecting channels, the occurring crystal phases can be determined by considering the present atomic planes and determining the interplanar spacing d of the samples using a fast Fourier transformation (FFT) calculation. The latter is shown for both analyzed films in Figure 12a,b. These FFT patterns reveal the presence of $Ce_{0.5}Zr_{0.5}O_2$, as the brightest circle has an interplanar spacing d of 0.305 nm, which can be assigned to the (111) reflection of the tetragonal crystal structure. Furthermore, the sample exposed to 150 ALD cycles features an additional diffraction ring, which was measured to possess an interplanar spacing d = 0.350 nm, which corresponds to the (011) reflection of anatase.

According to the ToF-SIMS results, there is no further impregnation of the pores after 50 cycles (see Figure 5). Therefore, we conclude that for the samples after 50 ALD cycles, the existent TiO$_x$ inside the mesopores is indeed crystalline TiO$_2$ in the anatase crystal structure.

CONCLUSIONS

This work summarizes different characterization methods to identify and characterize the infiltration of TiO$_2$ into an ordered mesoporous $Ce_{0.5}Zr_{0.5}O_2$ structure using ALD. It was verified by ToF-SIMS and ellipsometric investigations that TiO$_2$ was deposited into the mesopores up to 50 ALD cycles, followed by the formation of a top layer of TiO$_2$ for subsequent cycles, still maintaining observable pore sizes of
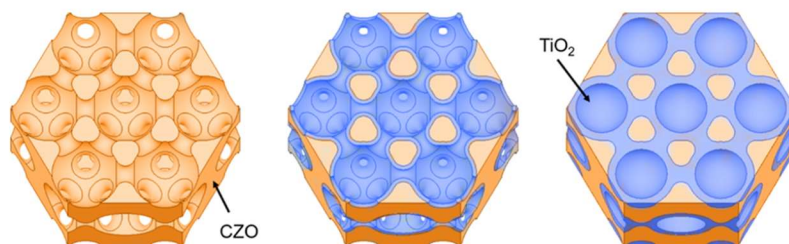
Figure 13. Schematic model of the TiO$_2$ deposition in the mesoporous CZO film using ALD. TiO$_2$ covers the surface of the 13 nm mesopores as well as the smaller interconnecting channel leading to a decrease in the average pore size. At a certain number of ALD cycles, the channels are completely filled, preventing the gaseous precursor to reach the inner pore layers while still retaining pores in the topmost pore layer.

around 10 nm detectable in SEM images. While XRD does not clarify the existing crystal structure of TiO$_2$ inside the pores, the FFT of HRSTEM images proves the deposited anatase structure. EDX measurements of the mesoporous film verified additionally the complementary distribution of CZO and TiO$_2$. The complete procedure is schematized in Figure 13. The catalytic performance of the herein prepared CZO/TiO$_2$ mesoporous thin films depending on the TiO$_2$ layer thickness will be addressed in upcoming studies.

All in all, this case study shows the successful deposition of an active species inside a mesoporous network by using ex situ characterization techniques and serves therefore as a guideline for future atomic layer depositions for different metal oxides into complex, porous substrates.

REFERENCES

(1) Miller, D. R.; Akbar, S. A.; Morris, P. A. Nanoscale Metal Oxide-Based Heterojunctions for Gas Sensing: A Review. *Sens. Actuators, B* **2014**, *204*, 250−272.

(2) Quackenbush, N. F.; Paik, H.; Woicik, J. C.; Arena, D. A.; Schlom, D. G.; Piper, L. F. J. X-Ray Spectroscopy of Ultra-Thin Oxide/Oxide Heteroepitaxial Films: A Case Study of Single-Nanometer VO$_2$/TiO$_2$. *Materials* **2015**, *8*, 5452−5466.

(3) Morgan, P. E. D.; Marshall, D. B. Functional Interfaces for Oxide/Oxide Composites. *Mater. Sci. Eng., A* **1993**, *162*, 15−25.

(4) Shi, J. On the Synergetic Catalytic Effect in Heterogeneous Nanocomposite Catalysts. *Chem. Rev.* **2013**, *113*, 2139−2181.

(5) Xu, Z.; Yu, L.; Xu, X.; Miao, J.; Jiang, Y. Effect of Oxide/Oxide Interface on Polarity Dependent Resistive Switching Behavior in ZnO/ZrO$_2$ Heterostructures. *Appl. Phys. Lett.* **2014**, *104*, No. 192903.

(6) Jiang, R.; Tung, S. o.; Tang, Z.; Li, L.; Ding, L.; Xi, X.; Liu, Y.; Zhang, L.; Zhang, J. A Review of Core-Shell Nanostructured Electrocatalysts for Oxygen Reduction Reaction. *Energy Storage Mater.* **2018**, *12*, 260−276.

(7) Trovarelli, A.; de Leitenburg, C.; Boaro, M.; Dolcetti, G. The Utilization of Ceria in Industrial Catalysis. *Catal. Today* **1999**, *50*, 353−367.

(8) Ahn, S. H.; Lee, N.; Choi, C.; Shin, S. W.; Han, Y.; Park, H. C. Feasibility Study of Fe$_3$O$_4$/TaO$_x$ Nanoparticles as a Radiosensitizer for Proton Therapy. *Phys. Med. Biol.* **2018**, *63*, No. 114001.

(9) Zhong, C. J.; Maye, M. M. Core-Shell Assembled Nanoparticles as Catalysts. *Adv. Mater.* **2001**, *13*, 1507−1511.

(10) Artiglia, L.; Agnoli, S.; Paganini, M. C.; Cattelan, M.; Granozzi, G. Core-Shell Nanoparticles as Artificial Enzymes with Peroxidase-Like Activity. *ACS Appl. Mater. Interfaces* **2014**, *6*, 20130−20136.

(11) Agnoli, S.; Reeder, A. E.; Senanayake, S. D.; Hrbek, J.; Rodriguez, J. A. Structure and Special Chemical Reactivity of Interface-Stabilized Cerium Oxide Nanolayers on TiO$_2$(110). *Nanoscale* **2014**, *6*, 800−810.

(12) Bai, J.; Sun, X.; Han, G.; Diao, G. Double-Shell CeO$_2$@TiO$_2$ Hollow Spheres Composites with Enhanced Light Harvesting and Electron Transfer in Dye-Sensitized Solar Cells. *J. Alloys Compd.* **2017**, *722*, 864−871.

(13) Saqer, S. M.; Kondarides, D. I.; Verykios, X. E. Catalytic Oxidation of Toluene over Binary Mixtures of Copper, Manganese and Cerium Oxides Supported on γ-Al$_2$O$_3$. *Appl. Catal., B* **2011**, *103*, 275−286.

(14) Saqer, S. M.; Kondarides, D. I.; Verykios, X. E. Catalytic Activity of Supported Platinum and Metal Oxide Catalysts for Toluene Oxidation. *Top. Catal.* **2009**, *52*, 517−527.

(15) Liu, R.; Duay, J.; Lee, S. B. Heterogeneous Nanostructured Electrode Materials for Electrochemical Energy Storage. *Chem. Commun.* **2011**, *47*, 1384−1404.

(16) Nong, H. N.; Oh, H. S.; Reier, T.; Willinger, E.; Willinger, M. G.; Petkov, V.; Teschner, D.; Strasser, P. Oxide-Supported IrNiO$_x$ Core-Shell Particles as Efficient, Cost-Effective, and Stable Catalysts

for Electrochemical Water Splitting. *Angew. Chem., Int. Ed.* **2015**, *54*, 2975−2979.

(17) Moser, M.; Mondelli, C.; Schmidt, T.; Girgsdies, F.; Schuster, M. E.; Farra, R.; Szentmiklósi, L.; Teschner, D.; Pérez-Ramírez, J. Supported CeO$_2$ catalysts in Technical Form for Sustainable Chlorine Production. *Appl. Catal., B* **2013**, *132−133*, 123−131.

(18) Huang, H.; Gong, H.; Chow, C. L.; Guo, J.; White, T. J.; Tse, M. S.; Tan, O. K. Low-Temperature Growth of SnO$_2$ Nanorod Arrays and Tunable n-p-n Sensing Response of a ZnO/SnO$_2$ heterojunction for Exclusive Hydrogen Sensors. *Adv. Funct. Mater.* **2011**, *21*, 2680−2686.

(19) He, Y. B.; Li, G. R.; Wang, Z. L.; Su, C. Y.; Tong, Y. X. Single-Crystal ZnO Nanorod/Amorphous and Nanoporous Metal Oxide Shell Composites: Controllable Electrochemical Synthesis and Enhanced Supercapacitor Performances. *Energy Environ. Sci.* **2011**, *4*, 1288−1292.

(20) Pagán-Torres, Y. J.; Gallo, J. M. R.; Wang, D.; Pham, H. N.; Libera, J. A.; Marshall, C. L.; Elam, J. W.; Datye, A. K.; Dumesic, J. A. Synthesis of Highly Ordered Hydrothermally Stable Mesoporous Niobia Catalysts by Atomic Layer Deposition. *ACS Catal.* **2011**, *1*, 1234−1245.

(21) Obaidat, I. M.; Nayek, C.; Manna, K. Investigating the Role of Shell Thickness and Field Cooling on Saturation Magnetization and Its Temperature Dependence in Fe$_3$O$_4$/γ-Fe$_2$O$_3$ Core/Shell Nanoparticles. *Appl. Sci.* **2017**, *7*, 1269.

(22) Burkett, S. L.; Sims, S. D.; Mann, S. Synthesis of Hybrid Inorganic-Organic Mesoporous Silica by Co-Condensation of Siloxane and Organosiloxane Precursors. *Chem. Commun.* **1996**, 1367−1368.

(23) Aronson, B. J.; Blanford, C. F.; Stein, A. Solution-Phase Grafting of Titanium Dioxide onto the Pore Surface of Mesoporous Silicates: Synthesis and Structural Characterization. *Chem. Mater.* **1997**, *9*, 2842−2851.

(24) Maschmeyer, T.; Rey, F.; Sankar, G.; Thomas, J. M. Heterogeneous Catalysts Obtained by Grafting Metallocene Complexes onto Mesoporous Silica. *Nature* **1995**, *378*, 159−162.

(25) Jiang, S. P. A Review of Wet Impregnation - an Alternative Method for the Fabrication of High Performance and Nano-Structured Electrodes of Solid Oxide Fuel Cells. *Mater. Sci. Eng., A* **2006**, *418*, 199−210.

(26) González Vargas, O. A.; De Los Reyes Heredia, J. A.; Montesinos Castellanos, A.; Chen, L. F.; Wang, J. A. Cerium Incorporating into MCM-41 Mesoporous Materials for CO Oxidation. *Mater. Chem. Phys.* **2013**, *139*, 125−133.

(27) O'Neill, B. J.; Jackson, D. H. K.; Lee, J.; Canlas, C.; Stair, P. C.; Marshall, C. L.; Elam, J. W.; Kuech, T. F.; Dumesic, J. A.; Huber, G. W. Catalyst Design with Atomic Layer Deposition. *ACS Catal.* **2015**, *5*, 1804−1825.

(28) Mahurin, S.; Bao, L.; Yan, W.; Liang, C.; Dai, S. Atomic Layer Deposition of TiO$_2$ on Mesoporous Silica. *J. Non-Cryst. Solids* **2006**, *352*, 3280−3284.

(29) Alibabaei, L.; Farnum, B. H.; Kalanyan, B.; Brennaman, M. K.; Losego, M. D.; Parsons, G. N.; Meyer, T. J. Atomic Layer Deposition of TiO$_2$ on Mesoporous NanoITO: Conductive Core−Shell Photoanodes for Dye-Sensitized Solar Cells. *Nano Lett.* **2014**, *14*, 3255−3261.

(30) Marizy, A.; Roussel, P.; Ringuedé, A.; Cassir, M. Atomic Layer Deposition of Epitaxial CeO$_2$ Thin Layers for Faster Surface Hydrogen Oxidation and Faster Bulk Ceria Reduction/Reoxidation. *J. Mater. Chem. A* **2015**, *3*, 10498−10503.

(31) George, S. M. Atomic Layer Deposition: An Overview. *Chem. Rev.* **2010**, *110*, 111−131.

(32) Berland, B. S.; Gartland, I. P.; Ott, A. W.; George, S. M. In Situ Monitoring of Atomic Layer Controlled Pore Reduction in Alumina Tubular Membranes Using Sequential Surface Reactions. *Chem. Mater.* **1998**, *10*, 3941−3950.

(33) Cameron, M. A.; Gartland, I. P.; Smith, J. A.; Diaz, S. F.; George, S. M. Atomic Layer Deposition of SiO$_2$ and TiO$_2$ in

(34) Pellin, M. J.; Stair, P. C.; Xiong, G.; Elam, J. W.; Birrell, J.; Curtiss, L.; George, S. M.; Han, C. Y.; Iton, L.; Kung, H.; et al. Mesoporous Catalytic Membranes: Synthetic Control of Pore Size and Wall Composition. *Catal. Lett.* **2005**, *102*, 127−130.

(35) Reitz, C.; Breitung, B.; Schneider, A.; Wang, D.; Von Der Lehr, M.; Leichtweiss, T.; Janek, J.; Hahn, H.; Brezesinski, T. Hierarchical Carbon with High Nitrogen Doping Level: A Versatile Anode and Cathode Host Material for Long-Life Lithium-Ion and Lithium-Sulfur Batteries. *ACS Appl. Mater. Interfaces* **2016**, *8*, 10274−10282.

(36) Sree, S. P.; Dendooven, J.; Korányi, T. I.; Vanbutsele, G.; Houthoofd, K.; Deduytsche, D.; Detavernier, C.; Martens, J. A. Aluminium Atomic Layer Deposition Applied to Mesoporous Zeolites for Acid Catalytic Activity Enhancement. *Catal. Sci. Technol.* **2011**, *1*, 218−221.

(37) Kraffert, K.; Karg, M.; Schmack, R.; Clavel, G.; Boissiere, C.; Wirth, T.; Pinna, N.; Kraehnert, R. Stabilization of Mesoporous Iron Oxide Films against Sintering and Phase Transformations via Atomic Layer Deposition of Alumina and Silica. *Adv. Mater. Interfaces* **2018**, No. 1800360.

(38) Detavernier, C.; Dendooven, J.; Sree, S. P.; Ludwig, K. F.; Martens, J. A. Tailoring Nanoporous Materials by Atomic Layer Deposition. *Chem. Soc. Rev.* **2011**, *40*, 5242−5253.

(39) Dendooven, J.; Devloo-Casier, K.; Levrau, E.; Van Hove, R.; Pulinthanathu Sree, S.; Baklanov, M. R.; Martens, J. A.; Detavernier, C. In Situ Monitoring of Atomic Layer Deposition in Nanoporous Thin Films Using Ellipsometric Porosimetry. *Langmuir* **2012**, *28*, 3852−3859.

(40) Dendooven, J.; Goris, B.; Devloo-Casier, K.; Levrau, E.; Biermans, E.; Baklanov, M. R.; Ludwig, K. F.; Van Der Voort, P.; Bals, S.; Detavernier, C. Tuning the Pore Size of Ink-Bottle Mesopores by Atomic Layer Deposition. *Chem. Mater.* **2012**, *24*, 1992−1994.

(41) Dendooven, J.; Devloo-Casier, K.; Ide, M.; Grandfield, K.; Ludwig, K. F.; Van Der Voort, P.; Bals, S.; Detavernier, C. *In In Situ Characterization of ALD in Mesoporous Thin Films by Grazing Incidence Small Angle X-Ray Scattering*, 12th International Conference on Atomic Layer Deposition (ALD 2012), 2012; p 6605.

(42) Hartmann, P.; Lee, D.; Smarsly, B. M.; Janek, J. Mesoporous TiO$_2$: Comparison of Splitting Reaction. *ACS Nano* **2010**, *4*, 3147−3154.

(43) Sallard, S.; Schröder, M.; Boissière, C.; Dunkel, C.; Etienne, M.; Walcarius, A.; Oekermann, T.; Wark, M.; Smarsly, B. M. Bimodal Mesoporous Titanium Dioxide Anatase Films Templated by a Block Polymer and an Ionic Liquid: Influence of the Porosity on the Permeability. *Nanoscale* **2013**, *5*, 12316−12329.

(44) Von Graberg, T.; Hartmann, P.; Rein, A.; Gross, S.; Seelandt, B.; Röger, C.; Zieba, R.; Traut, A.; Wark, M.; Janek, J.; et al. Mesoporous Tin-Doped Indium Oxide Thin Films: Effect of Mesostructure on Electrical Conductivity. *Sci. Technol. Adv. Mater.* **2011**, *12*, No. 025005.

(45) Weidmann, C.; Brezesinski, K.; Suchomski, C.; Tropp, K.; Grosser, N.; Haetge, J.; Smarsly, B. M.; Brezesinski, T. Morphology-Controlled Synthesis of Nanocrystalline η-Al$_2$O$_3$ Thin Films, Powders, Microbeads, and Nanofibers with Tunable Pore Sizes from Preformed Oligomeric Oxo-Hydroxo Building Blocks. *Chem. Mater.* **2012**, *24*, 486−494.

(46) Cop, P.; Kitano, S.; Niinuma, K.; Smarsly, B.; Kozuka, H. In-Plane Stress Development in Mesoporous Thin Films. *Nanoscale* **2018**, *10*, 7002−7015.

(47) Lee, S. M.; Lee, H. H.; Hong, S. C. Influence of Calcination Temperature on Ce/TiO$_2$ catalysis of Selective Catalytic Oxidation of NH$_3$ to N$_2$. *Appl. Ca.tal., A* **2014**, *470*, 189−198.

(48) Shen, Y.; Zheng, D.; Yang, B.; Ni, S.; Zhu, S. Synergetic Catalysis of Ceria and Titania for Selective Reduction of NO. *J. Rare Earths* **2012**, *30*, 431−436.

(49) Fang, J.; Bi, X.; Si, D.; Jiang, Z.; Huang, W. Spectroscopic Studies of Interfacial Structures of CeO$_2$-TiO$_2$ Mixed Oxides. *Appl. Surf. Sci.* **2007**, *253*, 8952−8961.

(50) Huang, B.; Yu, D.; Sheng, Z.; Yang, L. Novel CeO_2@TiO_2 Core−shell Nanostructure Catalyst for Selective Catalytic Reduction of NO_x with NH_3. *J. Environ. Sci.* **2017**, *55*, 129−136.

(51) Wang, H.-F.; Li, H.-Y.; Gong, X.-Q.; Guo, Y.-L.; Lu, G.-Z.; Hu, P. Oxygen Vacancy Formation in CeO_2 and $Ce_{1−x}Zr_xO_2$ Solid Solutions: Electron Localization, Electrostatic Potential and Structural Relaxation. *Phys. Chem. Chem. Phys.* **2012**, *14*, 16521−16535.

(52) King, D. M.; Liang, X.; Zhou, Y.; Carney, C. S.; Hakim, L. F.; Li, P.; Weimer, A. W. Atomic Layer Deposition of TiO_2 Films on Particles in a Fluidized Bed Reactor. *Powder Technol.* **2008**, *183*, 356−363.

(53) Reiners, M.; Xu, K.; Aslam, N.; Devi, A.; Waser, R.; Hoffmann-Eifert, S. Growth and Crystallization of TiO_2 Thin Films by Atomic Layer Deposition Using a Novel Amido Guanidinate Titanium Source and Tetrakis-Dimethylamido-Titanium. *Chem. Mater.* **2013**, *25*, 2934−2943.

(54) Aarik, J.; Aidla, A.; Uustare, T.; Kukli, K.; Sammelselg, V.; Ritala, M.; Leskelä, M. Atomic Layer Deposition of TiO_2 Thin Films from TiI_4 and H_2O. *Appl. Surf. Sci.* **2002**, *193*, 277−286.

(55) Patterson, A. L. The Scherrer Formula for X-Ray Particle Size Determination. *Phys. Rev.* **1939**, *56*, 978−982.

(56) Pennycook, S. J.; Jesson, D. E. High-Resolution Z-Contrast Imaging of Crystals. *Ultramicroscopy* **1991**, *37*, 14−38.

(57) Fujiwara, H. *Spectroscopic Ellipsometry: Principles and Applications*, 1st ed.; John Wiley & Sons Inc.: Hoboken, New Jersey, 2007.

(58) Boissiere, C.; Grosso, D.; Lepoutre, S.; Nicole, L.; Bruneau, A. B.; Sanchez, C. Porosity and Mechanical Properties of Mesoporous Thin Films Assessed by Environmental Ellipsometric Porosimetry. *Langmuir* **2005**, *21*, 12362−12371.

(59) Brinker, C. J.; Lu, Y.; Sellinger, A.; Fan, H. Evaporation-Induced Self-Assembly: Nanostructures Made Easy. *Adv. Mater.* **1999**, *11*, 579−585.

(60) Brezesinski, T.; Antonietti, M.; Groenewolt, M.; Pinna, N.; Smarsly, B. The Generation of Mesostructured Crystalline CeO_2, ZrO_2 and CeO_2-ZrO_2 Films Using Evaporation-Induced Self-Assembly. *New J. Chem.* **2005**, *29*, 237−242.

(61) Aarik, J.; Aidla, A.; Mändar, H.; Uustare, T. Atomic Layer Deposition of Titanium Dioxide from $TiCl_4$ and H_2O: Investigation of Growth Mechanism. *Appl. Surf. Sci.* **2001**, *172*, 148−158.

(62) Langner, A.; Knez, M.; Müller, F.; Gösele, U. TiO_2 Microstructures by Inversion of Macroporous Silicon Using Atomic Layer Deposition. *Appl. Phys. A Mater. Sci. Process.* **2008**, *93*, 399−403.

(63) Peña-Rodríguez, O.; Sánchez-Valdés, C. F.; Garriga, M.; Alonso, M. I.; Obradors, X.; Puig, T. Optical Properties of Ceria-Zirconia Epitaxial Films Grown from Chemical Solutions. *Mater. Chem. Phys.* **2013**, *138*, 462−467.